COMMUNICATIONS
PHYSICS

ARTICLE

https://doi.org/10.1038/s42005-020-00411-4 OPEN

Check for updates

Topological transitions in superconductor nanomembranes under a strong transport current

R. O. Rezaev [1,2], E. I. Smirnova[1], O. G. Schmidt[1,3,4,5] & V. M. Fomin [1,6]✉

The topological defects, vortices in bulk superconductors (SCs) and phase slips in low-dimensional SCs are known to lead to the occurrence of a finite resistance. We report on a topological transition between the both types of topological defects under a strong transport current in an open SC nanotube with a submicron-scale inhomogeneity of the normal-to-the-surface component of the applied magnetic field. When the magnetic field is orthogonal to the axis of the nanotube, which carries the transport current in the azimuthal direction, the phase-slip regime is characterized by the vortex/antivortex lifetime $\sim 10^{-14}$ s versus the vortex lifetime $\sim 10^{-11}$ s for vortex chains in the half-tubes, and the induced voltage shows a pulse as a function of the magnetic field. The topological transition between the vortex-chain and phase-slip regimes determines the magnetic-field–voltage and current–voltage characteristics of curved SC nanomembranes to pursue high-performance applications in advanced electronics and quantum computing.

---

[1] Institute for Integrative Nanosciences, Leibniz IFW Dresden, Helmholtzstraße 20, D-01069 Dresden, Germany. [2] Tomsk Polytechnic University, Lenin av. 30, 634050 Tomsk, Russia. [3] Material Systems for Nanoelectronics, TU Chemnitz, Reichenhainer Straße 70, D-09107 Chemnitz, Germany. [4] Research Center for Materials, Architectures and Integration of Nanomembranes (MAIN), TU Chemnitz, Rosenberg Straße 6, D-09126 Chemnitz, Germany. [5] Nanophysics, Faculty of Physics, TU Dresden, Nöthnitzer Straße 61, D-01187 Dresden, Germany. [6] Institute of Engineering Physics for Biomedicine, National Research Nuclear University MEPhI, Kashirskoe shosse 31, 115409 Moscow, Russia. ✉email: v.fomin@ifw-dresden.de

Topological defects in a superconductor, where the order parameter locally vanishes and its phase has no definite value, lead to the emergence of a finite resistance: “the superconductor is no longer ‘superconducting’ in a practical sense: it offers resistivity to the current!”[1]. The most well-known topological defects are vortices (antivortices) in a bulk superconductor, where the superconducting order parameter decreases from a certain value in the region far from a defect to zero on a line called vortex core[2]. The phase of the order parameter is not defined on the vortex core. When encircling a vortex core, the phase of the order parameter changes by $\pm 2\pi$ for ordinary vortices/antivortices or by an integer multiple of $\pm 2\pi n$ ($n = 2, 3\ldots$) for giant vortices/antivortices.

Under certain circumstances, topological defects occur in confined superconductor structures. The total phase advance by a multiple of 2π around a topological defect is called phase slip. The concept of the phase slippage in the resistive state of the narrow (quasi-1D) superconductor filaments was introduced in ref. [3]. At the phase-slip event, both real and imaginary parts of the superconducting order parameter vanish at a point along the filament. The analysis in ref. [3] was based on the thermal-fluctuation-dominated regime of the occurrence of phase slips near the critical temperature. Fluctuation-driven phase slips may be considered as a sequence of the events of local vanishing and local reappearance of the order parameter. Following[4], let us assume, that in a quasi-1D superconductor carrying transport current just below the critical temperature, there occurs a weak link (a domain of weakened superconductivity). In case if the transport current is slightly increased, the superconducting state vanishes in the weak-link domain. In the next instance, the weak-link domain reveals normal conductivity mediated by unpaired electrons, whose drift velocity is reduced by inelastic scattering. As long as there are unpaired electrons below the critical temperature with a drift velocity smaller than the critical velocity of the condensate, those electrons condense into Cooper pairs, which are accelerated to carry the current as a supercurrent, and the process repeats again.

Later, other mechanisms of phase slips were developed. In particular, inhomogeneity of a superconductor filament[5] makes its critical current inhomogeneous, so that an increase in the transport current leads to a local collapse of the order parameter. The current must be then entirely carried as the normal current. This allows superconductivity to reappear, and the cycle repeats due to the relaxation oscillation of the order parameter[5]. For low temperatures <0.2 K, the behavior of a 1D superconductor was shown to be dominated by quantum mechanical tunneling through the free-energy barrier: quantum phase slips[6]. An experimental evidence for a quantum phase transition driven by the quantum fluctuations in a two-dimensional (2D) superconductor has been recently obtained through magnetotransport measurements[7].

A further insight in the phase-slip phenomenon was gained for 2D and quasi-2D superconductors. For nanowires of 100 nm width (nanostripes), it was shown[8,9] that at relatively low current densities, the 1D Langer–Ambegaokar–McCumber–Halperin mechanism[3,10] based on thermally induced phase-slip centers dominated over the 2D mechanism related to unbinding of vortex–antivortex pairs below the Berezinskii–Kosterlitz–Thouless (BKT) transition in 2D[11–13]. At temperatures above the BKT critical temperature up until the critical temperature, thermal fluctuations are sufficient to unbind vortex–antivortex pairs, while below the BKT critical temperature all vortices are tightly bound into vortex–antivortex pairs[14]. The effect of the magnetic-field-induced BKT scenario was observed in a 2D spin-dimer system by using a multilayer magnet[15]. Another example of a phase transition in superconducting vortex systems is a liquid–solid transition experimentally found in 2D geometry[16]. A BKT-type crossover was detected in a trapped quantum degenerate gas of rubidium atoms[17]. The experimental signatures of quantum phase slips were the observation of temperature-independent dissipation for a Bose–Einstein condensate in a 3D optical lattice[18] and of velocity-dependent dissipation for an ultracold quantum gas in a 1D optical lattice[19]. The crossover from thermal to quantum phase slips controlled by the velocity was detected in 1D superfluid tubes[20].

At weaker transport currents, dissipation below the critical temperature is attributed to thermally activated motion of the order parameter over the free-energy barriers, which separate metastable states. At stronger transport currents, the free energy required for unbinding a vortex–antivortex pair is reduced, and the corresponding thermally activated contribution to the resistivity is expected to be dominant. In this regime, the resistivity due to vortex flow is substantially affected by electron heating. In an external magnetic field, the situation changes drastically. Even in a weak magnetic field, the contribution of moving vortices dominates over the thermally activated phase-slip mechanism in the resistivity in superconducting wires of submicron width[8].

In novel superconductor nanostructured microarchitectures, e.g., open nanotubes[21,22] and nanocoils[23–25] in a magnetic field orthogonal to their axes, distribution of the order parameter over the surface is highly inhomogeneous. This opens up new possibilities for manifestations of phase slips as compared to quasi-1D filaments and quasi-2D stripes. In the nanohelices as small as 100 nm in diameter and aspect ratio up to 65, fingerprints of vortex and phase-slip patterns have been experimentally identified, and supported by numerical simulations based on the time-dependent Ginzburg–Landau (TDGL) equation[25].

In the present paper, we demonstrate that a transition between different patterns of vortices is accompanied by occurrence of a weak link at the side of a nanotube, which is opposite to the slit, giving rise to novel phase-slip events. We identify the structure of superconducting screening currents (SSCs) induced by an external magnetic field and show that curved superconductor nanoarchitectures provide a unique possibility to study the interplay of multiple disconnected regions of SSCs. The dynamics of topological defects (superconducting vortices and phase slips) and the topological transitions between different configurations of SSCs manifest themselves through current–voltage or magnetic-field–voltage characteristics. The induced voltage increases more than threefold on certain intervals of the magnetic field in Nb and Sn open nanotubes.

Results

The simplest example of multiple disconnected loops of SSC is the two loops of SSC (Fig. 1a), which can be realized experimentally in an open superconducting tube placed in a homogeneous magnetic field orthogonal to the tube’s axis (Fig. 1b). The 2D-cylindrical structure is convenient for the numerical study of the order parameter dynamics, since the mathematical model can be formulated in a way equivalent to the planar structure in an inhomogeneous magnetic field. The tube has a cut in the paraxial direction, which will hereinafter be referred to as “slit”. Two electrodes are attached to both edges of the slit (Fig. 1b), in order to support an azimuthal transport current. The width of the slit is supposed to be much smaller than the circumference $2\pi R$, and the electrodes extend along the entire length of the edges. The whole system is placed in the magnetic field $\mathbf{B} = B\mathbf{e_z}$, which induces SSCs (Meissner currents) circulating in each half-tube. Above the first critical magnetic field, the vortex pattern typical for the open tube is shown in Fig. 1c.

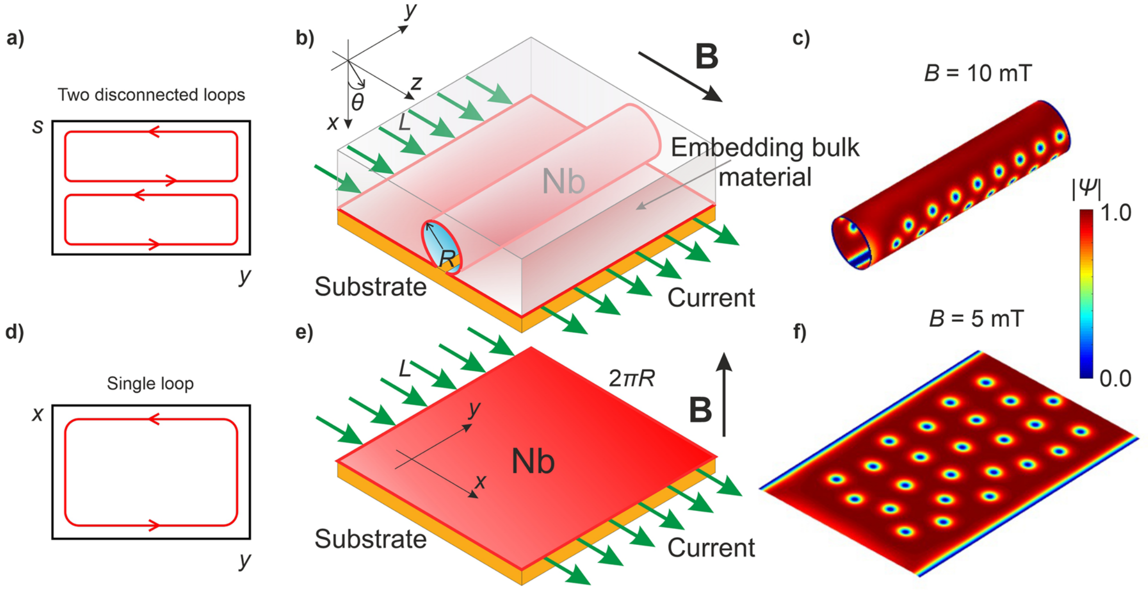

Fig. 1 SSCs and vortex patterns in the open tube in comparison to the planar structure. Scheme of the SSCs in the open tube represented on its surface (**a**). Scheme of the open tube embedded into the heat releasing bulk material (**b**). The y-axis is selected as the polar axis of cylindrical coordinates (ρ, θ, and y). The azimuthal angle θ is counted from the direction of the x-axis passing through the middle of the slit, the corresponding arc length is $s = R\theta$. The applied magnetic field $\mathbf{B} = B\mathbf{e_z}$ is directed along the z-axis for the tube. The transport current (green arrows) flows from the rear electrode over the cylindrical surface to the front electrode. Distribution of the modulus of the order parameter $|\psi|$ in the Nb open tube of radius 500 nm (**c**) (which is feasible within the focused electron-beam-induced deposition technology[37] and the focused ion-beam-induced deposition technology[25,32]). Vortices nucleate at the right edge, move in the direction opposite to the y-axis, and denucleate at the left edge in the front half-tube and vice versa in the rear half-tube. Schemes of the SSCs (**d**) represented on the surface of the corresponding Nb unrolled planar film (**e**) and distribution of the modulus of the order parameter $|\psi|$ (**f**).

The SSCs (Fig. 1d) in the planar structure (Fig. 1e) and the vortex pattern (Fig. 1f) are cardinally different from the SSCs (Fig. 1a) and the vortex pattern (Fig. 1c) in the open tube, correspondingly. The superconducting state is described by the TDGL equation for the complex-valued order parameter ψ coupled with the Poisson's equation (see "Methods" section). A rolled-up superconducting nanomembrane can be embedded fully and conformally in a polymer (Supplementary Fig. 1), i.e., varnish GE-7031, that has a thermal conductivity, which is about one order of magnitude higher than that of helium gas at low temperatures. This experimental concept can be used for efficient cooling of the superconductor and would then allow for higher current flows through the structure without overheating effects (Supplementary Note 1). The effects of the induced magnetic field are considered to be negligible[26] (Supplementary Figs. 2–4, Supplementary Note 2).

The modulus and phase of the order parameter, and the SSC patterns for the planar structure are represented in Fig. 2a–f, where the transport current is applied in the y-direction. The superconducting current after subtraction of the transport current is presented in Fig. 2c, f. Each vortex is a topoligical defect identified through the phase of the order parameter, while the phase-slip appearance is accompanied by the topological transition of SSCs. For the planar structure, the spacio-temporal analysis of the order parameter reveals a topological transition from one loop of SSCs (Fig. 2c) to three loops (Fig. 2f), when the phase slip appears. However, no topological changes are detected in the vortex dynamics, when the phase slip has appeared. The phenomenon of flux-flow instability that governs the occurrence of localized regions with suppressed superconductivity was described theoretically in a disordered thin superconducting strip in a homogeneous magnetic field[27]. In an open nanotube, we observe that a region of the fast-moving vortices (shown in Fig. 2g, h) near an edge transforms into a phase-slip region, which propagates to the opposite edge of the structure. Two loops of SSCs are demonstrated in Fig. 2i.

The phase-slip-induced topological transition of SSCs in a Nb open nanotube at $T/T_c = 0.95$ is shown in Fig. 3a–f, where two loops of SSCs transform into four loops. As distinct from the planar structure, this transition is associated with the topological changes in the vortex dynamics: vortex–antivortex pairs start to be generated at a frequency, which is about three orders of magnitude higher than that for vortex chains. The manifestation of topological nature of vortices is shown in Fig. 3a, d, which depict the phase of the order parameter. When encircling each vortex/antivortex core in a specific direction (for example, counterclockwise), the phase changes by $+2\pi$ for a vortex and by -2π for an antivortex (see the black and white circles in Fig. 3d). The spacio-temporal structure of the phase slip is thus topologically different from the trivial topology of the initial two loops of SSCs. The vortex–antivortex pairs generation has a striking similarity with the BKT transtion observed in 2D systems (XY-models). Our simulation shows that when the magnetic field increases, the superconducting state without a phase slip reenters the structure with a chain of moving vortices, which are then transformed into channels of fast-moving vortices (Fig. 3b, c). Such channels are supposed to be observed experimentally[28]. As a result of the sequence of transitions: vortex-chain state–phase-slip state–vortex-chain state, a voltage pulse (Fig. 3b) is expected to be observed in the open tube, while in the planar structure, a monotonic growth of the voltage as a function of the magnetic field occurs. Three regimes of the order parameter dynamics illustrated by Supplementary Movies 1–7: the vortex-chain motion before the phase slip (the vortex lifetime is ~1.1×10^{-11} s), the phase slip, and the vortex-chain motion after the phase slip (see also Supplementary Fig. 6, Supplementary Note 4).

In Fig. 4a–c, the modulus and phase of the order parameter, as well as the magnetic-field–voltage characteristic are represented

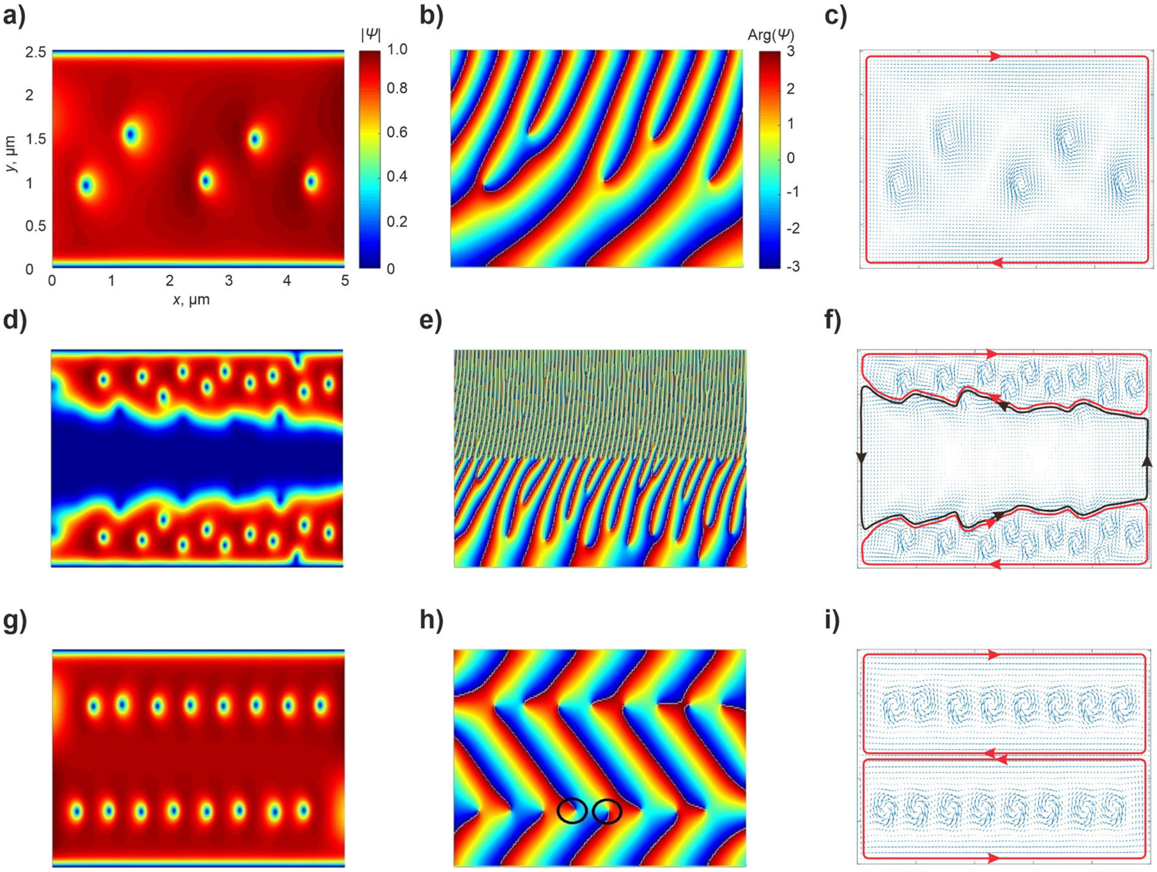

Fig. 2 Order parameter and SSCs in the planar structure in comparison to the open tube. The vortex, phase-slip, and SSC patterns in the Nb planar structure under the magnetic field 2 mT (**a**–**c**) and 14 mT (**d**–**f**), and in the open tube under the magnetic field 6 mT (**g**–**i**). In each row, the l.h.s, central and r.h.s panels represent, correspondingly, the modulus of the order parameter, the phase of the order parameter (the dimensionless phase of the order parameter Arg(ψ) changes from $-\pi$ to π), and the supercurrent density (blue arrows) encircled by the SSCs (bordeaux arrows). The SSCs form isolated loops with complex borders between them (**f**). In **h**, the vortex cores are marked with black circles. The asymmetry of phase distributions is due to the gauge choice (Supplementary Fig. 5, Supplementary Note 3).

for a Sn open nanotube at $T/T_c = 0.77$. The voltage derivative as a function of the magnetic field (Fig. 4d) emphasizes the beginning and end of the voltage peak.

Discussion

The obtained dynamics of the phase of the order parameter reflects the dynamics of kinematic vortex–antivortex pairs, first theoretically proposed in ref. [29] and experimentally detected in ref. [30] in planar microstructures. Kinematic vortex–antivortex pairs were shown[30] to have velocities higher than the Abrikosov vortex velocities. In refs. [29,31], kinematic vortex–antivortex pairs were numerically described under strong transport current (close to the critical value) at zero and weak magnetic fields. In the tubular structure (Fig. 1b), multiple kinematic vortex–antivortex pairs nucleate under strong transport current at the regions with zero and weak normal-to-surface component of the magnetic field. Remarkably, the green loops of SSCs in Fig. 3e connect front and rear half-tubes, thus introducing a new topology of the superconducting current. A topological transition from two disconnected regions of SSCs (red) to four (red and green) and then back to two (red) such regions occurs when increasing the magnetic field for certain intervals of values of the transport current. Under these conditions in open tubes, the nucleation locus connects both halves of the tube (Fig. 3e), as distinct from the previously known cases when kinematic vortex–antivortex pairs do not occur, and the both halves of the tube are strictly disconnected (Fig. 1a). Generation of the vortex–antivortex pairs marked with black and white circles in Fig. 3d (Supplementary Movie 4) results from (i) their unbinding due to the high transport current and (ii) motion due to the Magnus force caused by the magnetic field. Nucleation and separation of vortex–antivortex pairs at the side of the nanotube, which is opposite to the slit, are followed by their motion till (i) their denucleation at the sides of the tube or (ii) annihilation of a vortex from the pair with an antivortex from a neighboring pair (respectively, an antivortex from the pair with a vortex from another neighboring pair), when there exist two or more vortex–antivortex pairs. The relatively fast motion of the vortices and antivortices (with the vortex/antivortex lifetime ~9.6×10^{-15} s) on the side of the nanotube, which is opposite to the slit, leads to an apparent picture of an extended static phase slip (Fig. 3f). As follows from the comparison with the calculated vortex dynamics in an open tube (Supplementary Movie 1), the ratio of velocities for kinematic vortex–antivortex pairs and Abrikosov vortices is as large as about two orders of magnitude, what is close to that obtained for a Sn planar film[30].

The voltage generated in dc transport represents different order parameter states: the pure superconducting state, the mixed state (vortices and the superconducting state), the phase-slips states, and the normal state. A switching between those

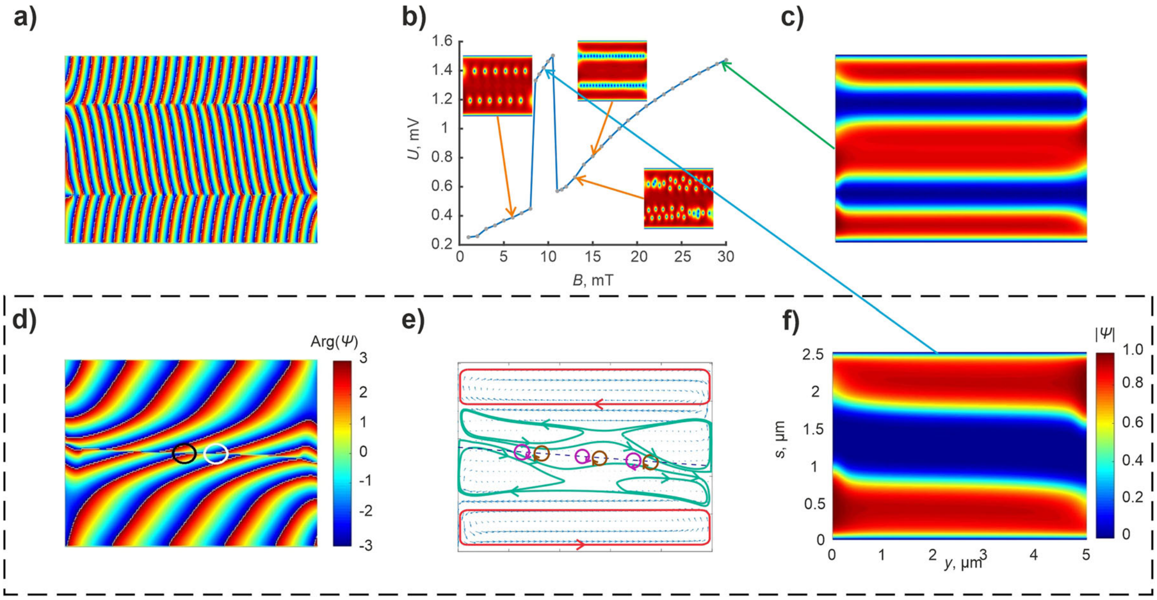

Fig. 3 Order parameter in the Nb open tube typical for different regimes of the magnetic-field-voltage characteristic. The phase (**a**) of the order parameter in a Nb nanotube of radius 400 nm under the applied magnetic field 30 mT. The voltage induced due to the moving vortices as a function of the magnetic field (**b**); distributions of the modulus of the order parameter for a few magnetic fields are shown in insets (Supplementary Movies 1–3). The modulus (**c**) of the order parameter in the same nanotube under the applied magnetic field 30 mT. The phase (**d**) of the order parameter, the streamlines of the superconducting current (**e**), and the modulus of the order parameter (**f**) in the same nanotube under the applied magnetic field 10 mT. Red lines in **e** are disconnected loops of SSCs flowing in both half-tubes. The current distribution within the phase-slip region (blue area in **f**) consists of two new disconnected loops (green lines in **e**), between which the (dashed) line of fast dynamics of vortex–antivortex pairs (burgundy and brown circles) occurs. All results are obtained at $T/T_c = 0.95$ for the transport current density $j_{tr} = 20$ GA m^{-2}.

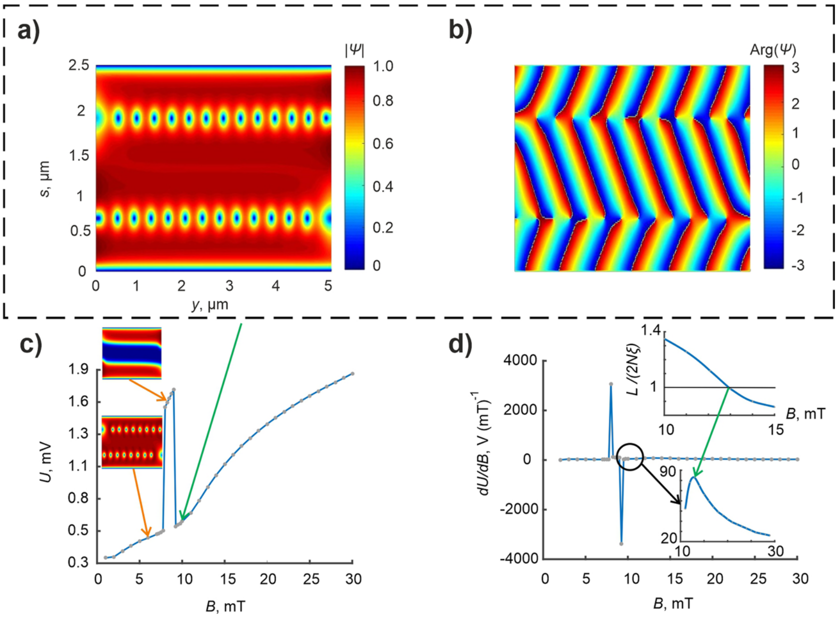

Fig. 4 Order parameter in the Sn open tube typical for different regimes of the magnetic-field-voltage characteristic. The modulus (**a**) and the phase (**b**) of the order parameter in a Sn nanotube of radius 400 nm under the applied magnetic field 9 mT. The voltage induced due to the moving vortices as a function of the magnetic field (**c**). The voltage derivative as a function of the magnetic field (**d**). The upper inset is the relative size of the interval per one vortex $L/(N/2)$ in a chain of $N/2$ vortices with respect to the characteristic dimension of a vortex $\sim 4\xi$. The lower inset is the zoomed plot of the voltage derivative in the magnetic field range from 10 mT to 30 mT. All results are obtained at $T/T_c = 0.77$ for the transport current density $j_{tr} = 17.54$ GA m^{-2}.

states corresponds to jumps in voltage as a function of the current or the magnetic field. The voltage pulse shown in Fig. 3b is calculated for the currents close to the critical ones (i.e., higher than $0.5\,J_c$). Within these values of parameters, the state of the order parameter is estimated to be very sensitive to the temperature.

The order parameter state in a Nb open nanotube is more sensitive to temperature variations in comparison with a Sn open

Table 1 Materials and geometrical parameters used for simulation (dirty limit[2] is used).

	Denotation	Value (for Nb)[22]	Value (for Sn)[34,35]
Penetration depth	$\lambda = \lambda_0\sqrt{\xi_0/(2.66l(1-T/T_c))}$	273 nm	269 nm Calculated from $\lambda_0 = 34$ nm[34] for the selected relative temperature.
Coherence length	$\xi = 0.855\sqrt{\xi_0 l/(1-T/T_c)}$	58 nm	66 nm Calculated from $\xi_0 = 230$ nm[34] for the selected relative temperature.
GL parameter	$\kappa = \lambda/\xi$	4.7	4.1
Fermi velocity	$v_F = \sqrt{2E_F/m_e}$	6×10^5 m s^{-1}	8×10^5 m s^{-1}[35]
Thickness of the film	d	50 nm	50 nm
Mean free electron path	l	6.0 nm	6.0 nm[36]
Diffusion coefficient	$D = lv_F/3$	1.2×10^{-3} m^2 s^{-1}	1.6×10^{-3} m^2 s^{-1}
Relative temperature	T/T_c	0.95	0.77
Normal conductivity for a thin membrane[22]	$\sigma = l/[3.72 \times 10^{-16}(\Omega\,\mathrm{m}^2)]$	16 (μΩ m)$^{-1}$	16 (μΩ m)$^{-1}$

nanotube (as follows from the comparison between Supplementary Figs. 7 and 8, see Supplementary Note 5). The temperature range, where the phase-slip regime exists, is wider for the Sn nanotube than for the Nb one: the voltage pulse in Nb occurs for temperature varying within 1% of T_c, while for Sn this temperature range is increased up to ~7% of T_c. The voltage derivative as a function of the magnetic field (Fig. 4c) demonstrates a relatively small peak for the case, when vortices with a characteristic dimension ~4ξ each form a chain, with a length just equal to the length L of the tube.

A nontrivial superconducting currents topology induces the phase-slip dynamics, which determine the voltage–magnetic field and voltage–current characteristics in nanoarchitectures, with multiple loops of SSCs. The spacio-temporal structure of the phase slips in an open tube and a planar structure is unveiled. The crucial difference between them lies in the vortex–antivortex pair generation in the open tube. The non-monotonous magnetic-field–voltage and current–voltage characteristics imply a possibility to efficiently tailor the superconducting properties of nanostructured materials by inducing a nontrivial topology of SSCs. The topological transition between the vortex-chain and phase-slip regimes opens up new perspectives for the advanced technological applications of rolled-up superconductor nanoarchitectures, such as for high-performance detectors and sensors, energy-storage components, quantum computing, and microwave radiation detection. It is also of heuristic importance for understanding of the phase-slip phenomena in confined low-dimensional superfluids.

Methods

The system is placed in the applied magnetic field $\mathbf{B} = B\mathbf{e_z}$, which induces SSCs (Meissner currents) circulating in each half-tube. The superconducting state is described by the TDGL equation for the complex-valued order parameter ψ in the dimensionless form (Tables 1 and 2):

$$\frac{\partial\psi}{\partial t} = -\left(\frac{1}{i\kappa}\nabla - \mathbf{A}\right)^2\psi + (1-|\psi|^2)\psi - i\kappa\varphi\psi, \tag{1}$$

where $\mathbf{A}$ is the vector potential; φ the scalar potential and $\kappa = \lambda/\xi$ the Ginzburg–Landau parameter with the London penetration depth λ and the coherence length ξ. Boundary conditions follow from the absence of the normal component of the superconducting current at the free boundaries of the superconductor:

$$\left(\mathbf{n}, \frac{1}{i\kappa}\nabla - \mathbf{A}\right)\psi\bigg|_{\partial D_s} = 0; \left(\mathbf{n}, \frac{1}{i\kappa}\nabla - \mathbf{A}\right)\psi\bigg|_{\partial D_y} = 0. \tag{2}$$

On the site of the electrodes, the boundary condition $\psi = 0$ can be used at the superconductor–normalmetal boundary (see, for example, ref. [32]). In order to check how boundary conditions may influence the order parameter dynamics, we considered several possibilities (Supplementary Fig. 9, Supplementary Note 6). We found that the voltage peak occurs in all cases.

Table 2 Dimensionless units used for Eqs. (7) and (8).

	Unit	Value (for Nb)	Value (for Sn)
Time	ξ^2/D	2.8 ps	2.7 ps
Length	λ	273 nm	269 nm
Magnetic field	$\Phi_0/[2\pi\lambda\xi]$	20.6 mT	18.5 mT
Current density	$\hbar c^2/[8\pi\lambda^2\xi e]$	60 GA m^{-2}	55 GA m^{-2}
Electric potential	$\sqrt{2}H_c\lambda^2/c\tau$	540 μV	484 μV
Conductivity	$c^2/[4\pi\kappa^2 D]$	31 (μΩ m)$^{-1}$	30 (μΩ m)$^{-1}$

The scalar potential φ is found as a solution of the Poisson's equation coupled with Eqs. (1) and (2):

$$\Delta\varphi = \frac{1}{\sigma}(\nabla, \mathbf{j}_{sc}), \tag{3}$$

where the superconducting current density is $\mathbf{j}_{sc} = \frac{1}{2i\kappa}(\psi^*\nabla\psi - \psi\nabla\psi^*) - \mathbf{A}|\psi|^2$ and σ is the normal conductivity. The transport current density $j_{tr}(y) = \mathrm{const} = j_{tr}$ is imposed via the boundary conditions for Eq. (3) at the edges of the slit, to which the electrodes are attached:

$$(\mathbf{n}, \nabla)\varphi|_{\partial D_s} = -\frac{1}{\sigma}j_{tr}; (\mathbf{n}, \nabla)\varphi|_{\partial D_y} = 0. \tag{4}$$

The vector potential with components $A_s(s, y)$ and $A_y(s, y)$ (where $s \equiv R\theta$) is chosen in the Coulomb gauge (the influence of the gauge choice on the vortex dynamics is discussed in Supplementary Fig. 5 and Supplementary Note 3):

$$A_s(s, y) = 0; A_y(s, y) = -BR\cos\left(\frac{s}{R}\right). \tag{5}$$

In order to guarantee the gauge invariance of the solution, we use link variables[33]:

$$U_s = \exp\left(-\int_{s_0}^{s} i\kappa A_s(\chi, y)d\chi\right); U_y = \exp\left(-\int_{y_0}^{y} i\kappa A_y(s, y)dy\right). \tag{6}$$

Then the set of Eqs. (1)–(4) takes the form:

$$\begin{aligned} &\Delta\varphi = \frac{1}{2\sigma\kappa}\sum_{\mu=s,y}\mathrm{Im}\left(\psi^* U_\mu^* \frac{\partial^2}{\partial\mu^2}[\psi U_\mu] - \psi U_\mu \frac{\partial^2}{\partial\mu^2}[\psi^* U_\mu^*]\right); \\ &\frac{\partial\varphi}{\partial s}\bigg|_{\partial D_s} = -\frac{1}{\sigma}j_{\mathrm{tr}}; \frac{\partial\varphi}{\partial y}\bigg|_{\partial D_y} = 0, \end{aligned} \tag{7}$$

$$\begin{aligned} &\frac{\partial\psi}{\partial t} = \frac{1}{\kappa^2}\sum_{\mu=s,y}\left(U_\mu^* \frac{\partial^2}{\partial\mu^2}[\psi U_\mu]\right) + (1-|\psi|^2)\psi - i\kappa\varphi\psi; \\ &\psi|_{t=0} = \Psi(s, y); \frac{\partial}{\partial s}[\psi U_s]\bigg|_{\partial D_s} = 0; \frac{\partial}{\partial y}[\psi U_y]\bigg|_{\partial D_y} = 0. \end{aligned} \tag{8}$$

We solve the set of Eqs. (7) and (8) numerically, using the relaxation method with a random ($|\psi|$ from the range [0, 1]) initial distribution of the order parameter $\psi(s, y)$. In the presence of the magnetic field ($B > B_{c1}$) and the transport current, it evolves toward a quasi-stationary state (Supplementary Movie 2). In the single-vortex-chain regime, the quasi-stationaly state is characterized by a periodic vortex nucleation and denucleation at the points on the edges, with the highest or the lowest component of the magnetic field normal-to-the-surface (see ref. [21]). Evaluations of temperature (the disorder) effects on the voltage peak survival are represented in Supplementary Figs. 7 and 8, and Supplementary Note 5 (Supplementary Fig. 10, Supplementary Note 7).

Vortices move paraxially along the tube. The moving vortices generate an electric field, which is opposite to the transport current density. We evaluate this field in terms of the voltage between the two electrodes shown in Fig. 1b, $\Delta\Phi = \varphi_1 - \varphi_2$. The scalar potential φ is found from the Poisson Eq. (3) with the boundary conditions Eq. (4). Finally, the following spacio-temporal averaging of the voltage is applied in line with the typical experimental situation (Supplementary Fig. 6):

$$U = \langle \Delta\Phi \rangle = \frac{1}{L_\Phi T}\int_0^T \int_0^{L_\Phi} [\varphi(s_1, y, t) - \varphi(s_2, y, t)]\mathrm{d}y\mathrm{d}t, \qquad (9)$$

where s_1 and s_2 are $\delta/2$ and $2\pi R - \frac{\delta}{2}$, correspondingly, δ is the slit width, L_Φ is the length of the averaging area (its maximal value is the length L of the tube), $T \gg \Delta t_1$ is the time of averaging, Δt_1 is the time required for a vortex to reach the opposite edge of a tube after nucleation[21].

Data availability

The video data that support the findings of this study are available in "figshare" repository with the identifier https://doi.org/10.6084/m9.figshare.12330986.v3.

Code availability

The codes that support the findings of this study are available from the corresponding author upon reasonable request.

Received: 5 March 2020; Accepted: 27 July 2020;
Published online: 20 August 2020

References

1. Kopnin, N. B. *Theory of Nonequilibrium Superconductivity* (Clarendon Press, Oxford, 2001).
2. Tinkham, M. *Introduction to Superconductivity* (McGraw-Hill, New York, 1996).
3. Langer, J. S. & Ambegaokar, V. Intrinsic resistive transition in narrow superconducting. *Channels Phys. Rev.* **164**, 498–510 (1967).
4. Tidecks, R. *Current-Induced Nonequilibrium Phenomena in Quasi-One-Dimensional Superconductors* (Springer, Berlin-Heidelberg, 1990).
5. Skocpol, J., Beasley, M. R. & Tinkham, M. Phase-slip centers and nonequilibrium processes in superconducting tin microbridges. *J. Low Temp. Phys.* **16**, 145–167 (1974).
6. Giordano, N. Evidence for macroscopic quantum tunneling in one-dimensional superconductors. *Phys. Rev. Lett.* **61**, 2137–2140 (1988).
7. Saito, Y., Nojima, T. & Iwasa, Y. Quantum phase transitions in highly crystalline two-dimensional superconductors. *Nat. Commun.* **9**, 778 (2018). 1–7.
8. Bell, M. et al. On the nature of resistive transition in disordered superconducting nanowires. *IEEE Trans. Appl. Sup.* **17**, 267–270 (2007).
9. Bell, M. et al. One-dimensional resistive states in quasi-two-dimensional superconductors: experiment and theory. *Phys. Rev. B* **76**, 094521 (2007). 1–5.
10. McCumber, D. E. & Halperin, B. I. Time scale of intrinsic resistive fluctuations in thin superconducting wires. *Phys. Rev. B* **1**, 1054–1070 (1970).
11. Berezinskii, V. S. Destruction of long-range order in one-dimensional and two-dimensional systems having a continuous symmetry group I. Classical systems. *Sov. Phys. JETP* **32**, 493–500 (1971).
12. Berezinskii, V. S. Destruction of long-range order in one-dimensional and two-dimensional systems having a continuous symmetry group II. Quantum systems. *Sov. Phys. JETP* **34**, 610–616 (1971).
13. Kosterlitz, J. M. & Thouless, D. J. Ordering, metastability and phase transitions in two-dimensional systems. *J. Phys. C* **6**, 1181–1203 (1973).
14. Halperin, B. I. & Nelson, D. R. Resistive transition in superconducting films. *J. Low Temp. Phys.* **36**, 599–616 (1979).
15. Tutsch, U. et al. Evidence of a field-induced Berezinskii-Kosterlitz-Thouless scenario in a two-dimensional spin-dimer system. *Nat. Commun.* **5**, 5169 (2014). 1–9.
16. Chen, B. et al. Two-dimensional vortices in superconductors. *Nat. Phys.* **3**, 239–242 (2007).
17. Hadzibabic, Z. et al. Berezinskii-Kosterlitz-Thouless crossover in a trapped atomic gas. *Nature* **441**, 1118–1121 (2006).
18. McKay, D., White, M., Pasienski, M. & DeMarco, B. Phase-slip-induced dissipation in an atomic Bose–Hubbard system. *Nature* **453**, 76–80 (2008).
19. Tanzi, L. et al. Velocity-dependent quantum phase slips in 1D atomic superfluids. *Sci. Rep.* **6**, 25965 (2016).
20. Scaffidi, S. A. et al. Exploring quantum phase slips in 1D bosonic systems. *Eur. Phys. J. Spec. Top.* **226**, 2815–2827 (2017).
21. Fomin, V. M., Rezaev, R. O. & Schmidt, O. G. Tunable generation of correlated vortices in open superconductor tubes. *Nano Lett.* **12**, 1282–1287 (2012).
22. Rezaev, R. O. et al. Voltage induced by superconducting vortices in open nanostructured microtubes. *Phys. Stat. Sol. RRL* **13**, 1–12 (2019).
23. Fomin, V. M. et al. Superconducting nanostructured microhelices. *J. Phys. Cond. Mat.* **29**, 395301 (2017). 1–9.
24. Lösch, S. et al. Microwave radiation detection with an ultra-thin free-standing superconducting niobium nanohelix. *ASC Nano* **13**, 2948–2955 (2019).
25. Córdoba, R. et al. Three-dimensional superconducting nano-helices grown by He$^+$-focused-ion-beam direct writing. *Nano Lett.* **19**, 8597–8604 (2019).
26. Smirnova, E. I., Rezaev, R. O. & Fomin, V. M. Simulation of dynamics of the order parameter in superconducting nanostructured materials: effect of the magnetic field renormalization. *Low Temp. Phys.* **46**, 325–331 (2020).
27. Vodolazov, D. Y. Flux-flow instability in a strongly disordered superconducting strip with an edge barrier for vortex entry. *Supercond. Sci. Technol.* **32**, 115013 (2019). 1–7.
28. Embon, L. et al. Imaging of super-fast dynamics and flow instabilities of superconducting vortices. *Nat. Commun.* **8**, 85 (2017). 1–10.
29. Andronov, A. et al. Kinematic vortices and phase slip lines in the dynamics of the resistive state of narrow superconductive thin film channels. *Phys. C* **213**, 193–199 (1993).
30. Sivakov, A. G. et al. Josephson behavior of phase-slip lines in wide superconducting strips. *Phys. Rev. Lett.* **91**, 267001 (2003). 1–4.
31. Berdiyorov, G. R., Milosevic, M. V. & Peeters, F. M. Kinematic vortex-antivortex lines in strongly driven superconducting stripes. *Phys. Rev. B* **79**, 184506 (2009). 1–8.
32. Córdoba, R. et al. Long-range vortex transfer in superconducting nanowires. *Sci. Rep.* **9**, 12386 (2019). 1–10.
33. Kato, R., Enomoto, Y. & Maekawa, S. Effects on the surface boundary on the magnetization process in type-II superconductors. *Phys. Rev. B* **47**, 8016–8024 (1993).
34. Parks, R. D. *Superconductivity* 1 (Marcel Dekker, New York-Basel, 1969).
35. Nakamura, Y. et al. Intrinsic charge transport in stanene: roles of bucklings and electron-phonon couplings. *Adv. Electron. Mater.* **3**, 1700143 (2017). 1–9.
36. Tanuma, S., Powell, C. J. & Penn, D. R. Calculations of electron inelastic mean free paths. IX. Data for 41 elemental solids over the 50 eV to 30 keV range. *Surf. Interface Anal.* **43**, 689–713 (2011).
37. Huth, M., Porrati, F. & Dobrovolskiy, O. V. Focused electron beam induced deposition meets materials science. *Microelectron. Eng.* **185-186**, 9–28 (2018).

Acknowledgements

The authors thank A. Bezryadin, J. Lorenzana, D. Roditchev, V. A. Shklovskij, H. Suderow, F. Tafuri, R. Tidecks, V. M. Vinokour, A. D. Zaikin, and E. Zeldov for fruitful discussions. The authors are grateful to DFG (Germany) for support under the Projects # FO 956/5-1, # FO 956/6-1, and to ZIH TU Dresden for providing its facilities for high-throughput calculations. V.M.F. acknowledges partial support within the framework of the COST Action CA16218 (NANOCOHYBRI) of the European Cooperation in Science and Technology, and through the MEPhI Academic Excellence Project (Contract # 02.a03.21.0005). R.O.R. thanks RFBR (Russia) and Tomsk Region for support through the research Project # 19-41-700004. Open access funding provided by Projekt DEAL.

Author contributions

V.M.F. led the project and conceived the investigations. R.O.R. and E.I.S. performed numerical simulations. O.G.S. and V.M.F. developed key conceptual ingredients for the physical interpretation. V.M.F. and R.O.R. wrote the manuscript. All authors contributed to discussions about the numerical modeling, the analysis of the obtained results, and the preparation of the final manuscript.

Competing interests

The authors declare no competing interests.

Additional information

Supplementary information is available for this paper at https://doi.org/10.1038/s42005-020-00411-4.

Correspondence and requests for materials should be addressed to V.M.F.

Reprints and permission information is available at http://www.nature.com/reprints

Publisher's note Springer Nature remains neutral with regard to jurisdictional claims in published maps and institutional affiliations.

Open Access This article is licensed under a Creative Commons Attribution 4.0 International License, which permits use, sharing, adaptation, distribution and reproduction in any medium or format, as long as you give appropriate credit to the original author(s) and the source, provide a link to the Creative Commons license, and indicate if changes were made. The images or other third party material in this article are included in the article's Creative Commons license, unless indicated otherwise in a credit line to the material. If material is not included in the article's Creative Commons license and your intended use is not permitted by statutory regulation or exceeds the permitted use, you will need to obtain permission directly from the copyright holder. To view a copy of this license, visit http://creativecommons.org/licenses/by/4.0/.

© The Author(s) 2020